EFFECT OF ROUGHNESS ON WALL-BOUNDED FLOWS SUBJECTED TO SPANWISE ROTATION

Ugo Piomelli[1], *Wen Wu*[2] *and Junlin Yuan*[3]

[1] *Queen's University, Kingston (ON) Canada*
[2] *Johns Hopkins University, Baltimore (MD) USA*
[3] *Michigan State University, East Lansing (MI) USA*

ugo@queensu.ca

Abstract

We performed direct simulations of channel flow subjected to rotation about a spanwise axis, comparing smooth walls and cases with random roughness. The destabilizing effect of roughness counteracts the stabilizing effect of rotation, on the cyclonic side, maintaining non-zero Reynolds shear stress at all rotation rates considered. The wake fluctuations result in significant dispersive stresses, which are attenuated by rotation on the cyclonic side. They, however, do not contribute significantly to the generation of turbulence. The instantaneous fields and spectra highlight the presence of elongated roll cells, which are not sensitive to the roughness. The sweeps and ejections responsible for a significant percentage of the Reynolds stress are due to motion whose coherence, in the wall normal direction, is increased, perhaps due to the roll cells.

1 Introduction

Wall-bounded flows subjected to rotation around the spanwise axis occur in a number of applications, the most common one being turbomachinery, such as the Francis turbine used in hydroelectric power plants. In a rotating frame of refence the Coriolis force, $\mathbf{\Omega} \times \mathbf{V}$ is added to the equations of motion. The Coriolis term can stabilize or destabilize the flow, depending on the value of the dimensionless rotation number ($Ro = -2\Omega/S$, where S is the mean shear), and on whether Ro and S have the same or opposite signs (see Durbin & Pettersson Reif (2001) for an extended discussion).

In a plane channel the mean shear has opposite signs on the two sides. For positive Ro, then, the lower wall (the pressure side) is subjected to anticyclonic rotation (Ro and S have the same sign) and the flow is de-stabilized (for moderate rotation rates), while on the upper, suction, side the rotation is cyclonic and the flow is stabilized. Thus, rotating flows of this type have been studied extensively. Johnston *et al.* (1972) and Kristoffersen & Andersson (1993) are among the first examples of(respectively) experimental and numerical studies of this problem. Other studies of this flow include the work by Tafti & Vanka (1991); Lamballais *et al.* (1996); Nakabayashi & Kitoh (1996); Lamballais *et al.* (1998); Maciel *et al.* (2003); Nakabayashi & Kitoh (2005); Grundestam *et al.* (2008); Xia *et al.* (2016). Given the difficulty of performing experiments of this type, most of these studies are numerical, and are conducted at low Reynolds number, $Re_\tau = u_\tau \delta/\nu \simeq 180$ (where u_τ is the friction velocity and δ the channel half-height).

Among the results of these investigations are: (1) a tendency to wards relaminarization on the cyclonic side at high Rotation numbers; (2) the formation of elongated longitudinal vortices and the enhancement of turbulence on the anticylonic side; (3) the longitudinal vortices may be responsible for strong (although infrequent) ejections that contribute to the Reynolds shear stress transport; (4) the mean velocity profile has a linear region with slope $2Ro_b$; in this layer the rms velocity fluctuations are also linear.

While these studies have considered smooth walls, in most flows of engineering interest the surfaces are rough; the effect of roughness is opposite to that of cyclonic rotation: notably, the Reynolds shear stress is increased and the Reynolds stress anisotropy is decreased. It is important, to predict the flow in practical application, to understand how these two opposite effects interact. Narasimhamurthy & Andersson (2015) considered ribbed channels subjected to spanwise rotation. The roughness was constituted by an array of square ribs, 40 wall units wide and high (the roughness height was one-tenth of the channel half-height), with a pitch equal to 8 times the roughness height. The nominal Reynolds number was $Re_\tau = 400$. With this pitch, the flow can reattach between ribs; this type of rough surface is known as k-type (Perry & Joubert, 1969), and the roughness used is probably in the transitionally rough regime. They found that the effect of rotation and roughness are, indeed, opposite on the cyclonic side. As in studies of the smooth-wall case, they found that the modification of the Reynolds stresses was also indirect, mainly occurring through the change in the velocity gradient, but also due to the effect of the Coriolis production.

In the present study we perform a simulation of rotating channel flows over smooth and rough wall using sandgrain roughness. The simulations are carried out

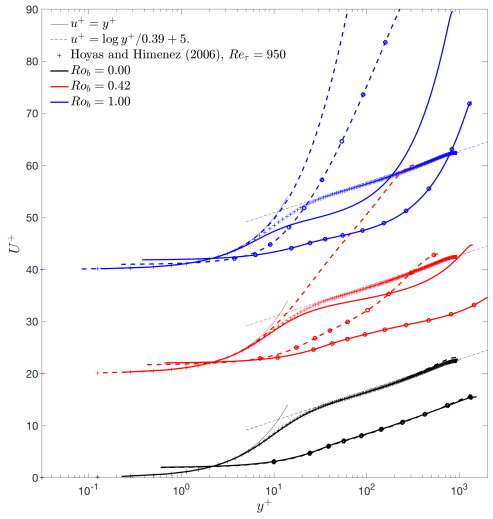

Figure 1: Mean velocity profiles in wall units. Lines: smooth wall. Lines with symbols: rough wall. Solid line: anti-cyclonic side; dashed: cyclonic side. The profiles are shifted by twenty units for clarity.

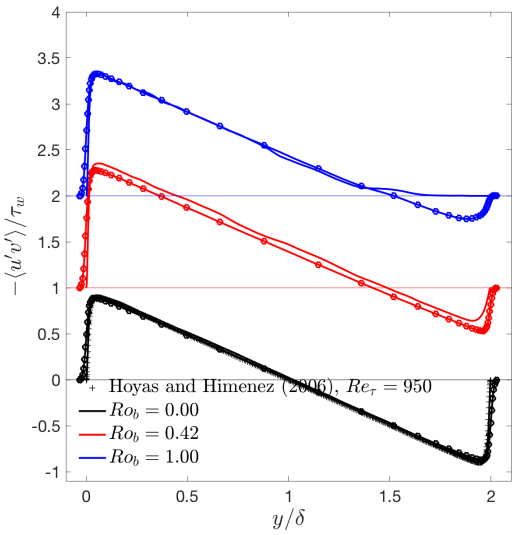

Figure 2: Reynolds shear stress profiles. Lines: smooth wall. Lines with symbols: rough wall. Solid line: anti-cyclonic side; dashed: cyclonic side. The profiles are shifted by one unit for clarity.

at $Re_\tau \simeq 1,000$, and the average roughness height is $k_{\rm avg} = 0.04\delta$. That allows us to reach the fully rough regime (at least on the anti-cyclonic side) while keeping the blockage very low. Furthermore, while ribbed channels are artificially generated, for instance to improve the cooling of turbines, sandgrain roughness is more representative of realistic surfaces encountered in many engineering applications, such as the blades of hydroelectric turbines.

2 Problem formulation

The equations of conservation of mass and momentum are solved:

$$\frac{\partial u_i}{\partial x_i} = 0 \tag{1}$$

$$\frac{\partial u_i}{\partial t} + \frac{\partial}{\partial x_k}(u_k u_i) = -\frac{1}{\rho}\frac{\partial P}{\partial x_i} + \nu\nabla^2 u_i - 2\epsilon_{i3k}\Omega_3 u_k + f_i. \tag{2}$$

Ω is the channel rotation rate, oriented in the spanwise direction. The forcing term f_i is used to enforce the no-slip boundary conditions inside the sandgrain roughness, modelled using an Immersed Boundary Method (IBM). The equations of motion are solved using second-order accurate (in time and space) derivatives on a staggered mesh. The code is parallelized using MPI, and has been widely validated in a variety of turbulent flows over smooth and rough surfaces.

Periodic boundary conditions are used in x and z. In the smooth-wall cases no-slip conditions are used in y; in the rough-wall ones, the IBM used is based on a Volume-of-Fluid technique (Scotti, 2006). Details of the numerical implementation of the IBM can be found in the original paper, or in Yuan & Piomelli (2014*a*).

We performed the direct numerical simulations at $Re_b = 19,000$ (based on channel height and average velocity); in the absence of rotation, this corresponds to $Re_\tau \simeq 1,000$ (based on channel half-height and friction velocity). The calculations were performed in a domain with dimensions $12 \times 2 \times 3$ (all lengths are normalized by the channel half-width δ) using $1536\times192\times384$ grid points for the smooth cases, and a domain with dimensions $12 \times 2 \times 6$ and $1536\times530\times768$ points for the rough ones. The mass-flow rate was kept constant, so that $Re_b = 19,000$ for all cases but Re_τ varied between 1,000 and 550 for the smooth-wall cases, and between 1,500 and 780 for the rough-wall ones. The code and the grid resolution used were validated by comparison with the DNS data of Hoyas & Jiménez (2006) for non-rotating smooth-wall cases, and with the low-Reynolds number calculations of Kristoffersen & Andersson (1993) for the cases with rotation. The agreement with the reference data for first- and second-order statistics and for the Reynolds stress budgets is very good. The roughness height was 4% of the channel half-height, small enough to avoid blockage effect, but sufficient to be in the fully rough regime ($k_s^+ \simeq 100 - 150$). Three rotation rates were examined: $Ro_b = 2\Omega\delta/U_b = 0$, 0.42 and 1.0.

3 Results and discussion

Figure 1 shows the mean velocity profiles, in inner units, for the six calculations. A logarithmic region is

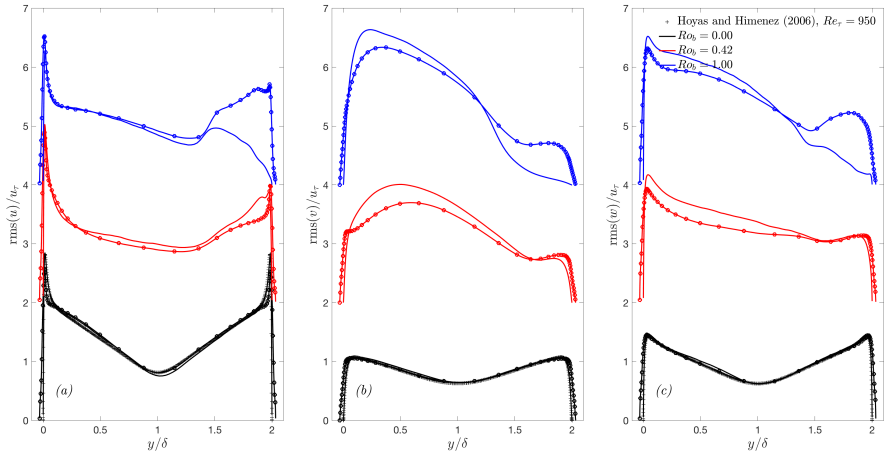

Figure 3: Root-mean-square velocity fluctuations. Lines: smooth wall. Lines with symbols: rough wall. The velocity profiles are shifted by two units for clarity.

observed on the unstable side, whose shift (the roughness function ΔU^+) is consistent for all cases, and is not strongly affected by the rotation rate. On the stable side no logarithmic layer is observed, either in the rough-wall or in the smooth-wall cases.

The Reynolds shear stresses are shown in Figure 2. Here, a prime denotes fluctuating quantities. A remarkable difference can be observed at the highest rotation rate: with a smooth wall, $\langle u'v' \rangle$ is negligible on the stable side, where the flow anisotropy increases as $\langle u'u' \rangle$ decreases less than $\langle v'v' \rangle$. When the wall is rough, on the other hand, the flow is more disturbed (as will be shown momentarily), resulting in a more turbulent-like profile.

Figure 3 shows the rms fluctuations. On the cyclonic side, the stabilizing effect of the rotation is significantly counterbalanced by the destabilization caused by the roughness. While on the stable side the rough-wall case is very different from the smooth-wall one, on the unstable side Townsend's similarity hypothesis seems to be valid: the rms fluctuations are independent of roughness, when scaled with the friction velocity, although u_τ is almost 50% higher in the rough-wall case.

Following Mignot *et al.* (2009), we can introduce a double-averaging approach to decompose a flow quantity into its time and space average, denoted by $\langle \cdot \rangle$, the spatial variation of the time average, $\widetilde{\cdot}$, also known as the wake field or the form-induced perturbation, and the stochastic turbulent fluctuation, denoted by a double prime:

$$\theta(x,y,z,t) = \langle \theta \rangle(y) + \widetilde{\theta}(x,y,z) + \theta''(x,y,z,t) \quad (3)$$

(and $\theta' = \widetilde{\theta} + \theta''$). The wake perturbations—such as $\partial \widetilde{u}_i / \partial x_j$ and $\widetilde{u_i'' u_j''}$—play an important role in the destabilization of the flow and in the redistribution of energy between the normal Reynolds stresses (Yuan & Piomelli, 2014*b*).

The $\widetilde{u}$, $\widetilde{v}$ and $\widetilde{p}$ wake components in planes near the walls are shown in Figure 4. In general, patterns of the wake velocity fluctuations are similar near both walls; rotation does not seem to play a major role in determining the wake-field pattern. The main difference between the two sides is the appearance of large regions of higher-magnitude, positive $\widetilde{u}$ on the stable side, and lower magnitudes (and possibly shorter coherence length) for $\widetilde{v}$ and $\widetilde{w}$ (not shown) on the stable side.

To quantify the magnitude of form-induced spatial perturbations, the components of the dispersive stress tensor are plotted in Figure 5. On both sides, the total kinetic energy of the wake fields remain significant, though weakened, with increasing Ro_b. The rotation attenuates the magnitudes of all components, which is more significant on the stable side, especially for the wall-normal, spanwise and shear components, whose drops in magnitude are 60–70%; this may be due to as yet unknown effects of rotation, or to the fact that the flow develops towards the transitionally rough regime. The roughness sublayer thickness—defined as the near-wall region where the form-induced perturbation is strong—appears insensitive to Ro_b. The non-negligible values of $\widetilde{u}$ above the roughness sublayer for the zero-Ro_b case are probably due to limitation in simulation time covered by the available data.

More interesting is the behaviour of the wake pressure $\widetilde{P}$, also shown in Figure 4. The time-averaged pressure distribution on the two sides are dramatically different. Recall that $\partial \widetilde{P} / \partial x$ contributes to pressure drag on the surface. On the unstable side, regions of negative and positive $\widetilde{P}$ are both of small sizes and appear frequently, leading to frequent pressure drag generation. On the stable side, however, large patches of negative $\widetilde{P}$ are present, with less frequent appearance of positive $\widetilde{P}$ region (compared to the unstable side); thus, the pressure drag generation occurs less frequently, resulting in lower u_τ. An important ques-

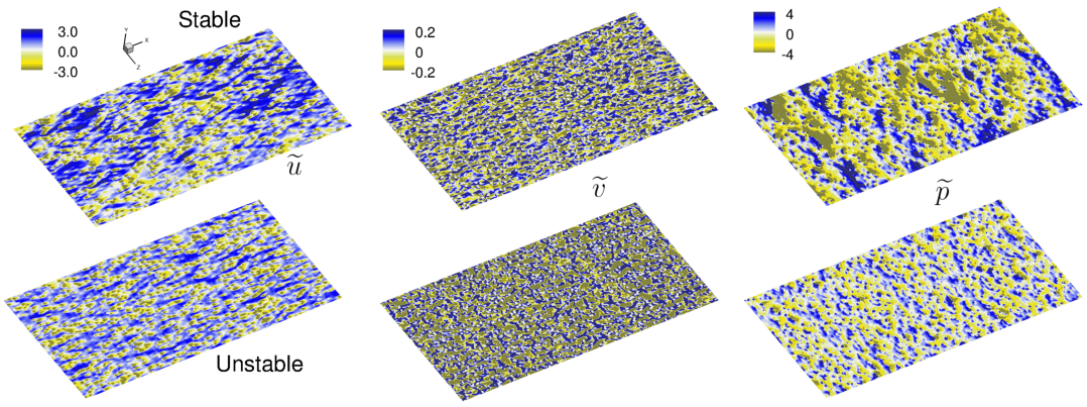

Figure 4: Contours of $\widetilde{u}$, $\widetilde{v}$ and $\widetilde{p}$ in planes 0.04δ away from both walls, normalized by local u_τ. Bottom: unstable side; top: stable side.

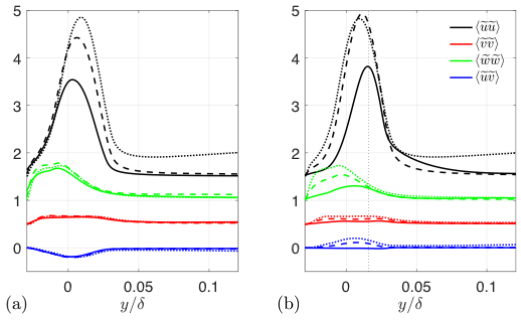

Figure 5: Dispersive stresses inside the roughness sublayer, normalized by local u_τ, on (a) unstable side and (b) stable side. - - - $Ro_b = 0.00$; – – – $Ro_b = 0.42$; ——— $Ro_b = 1.00$. Profiles are shifted upwards by 0.5 units for clarity.

tion, presently under investigation, is whether these patches are associated with large time-averaged recirculation regions due to the longitudinal roll cells characteristic of this flow (that will be discussed momentarily), which may shadow a large number of roughness elements so that they do not contribute to pressure drag.

Figure 6 shows an instantaneous picture of the flow, for the intermediate rotation number. Following Jeong & Hussain (1995), isosurfaces of λ_2 (the middle eigenvalue of the strain-rate tensor) are used to visualize the turbulent structures. They are normalized by the value of u_τ on the corresponding side of the channel. The quasi-laminarization on the cyclonic side when the wall is smooth is highlighted by the areas in which no turbulent activity is present. The rough-wall case shows a more homogeneous distribution of turbulent eddies. On the unstable side the structures tend to become aligned, forming very long trains, probably due to the long roll cells, observed experimentally (Johnston *et al.*, 1972) and numerically (Kristoffersen & Andersson, 1993).

To confirm this conjecture, we examined the premultiplied velocity spectra (not shown). Our findings agree with those of Brethouwer (2017): $k_z\Phi_{vv}$ shows the presence of energetic motions centred around $(y-d)/\delta = 0.5$, whose spanwise scale is the channel height, and that span the entire length of the channel. The spanwise spectrum of w, $k_z\Phi_{ww}$, shows two peaks, one above and one below the peak in $k_z\Phi_{vv}$, which may reflect the fact that v is strong between the rollers while w is dominant above and below them. The spectra for rough and smooth walls are very similar, indicating that the effect of the roughness does not propagate far enough from the wall to affect the roll cells.

In Figure 7 we show the conditionally averaged Reynolds shear stress. The occurrence of sweeps (fluid moving towards the wall) and ejections (fluid moving away from the wall) was used as the criterion for the averages. Events were detected by requiring that $|v'| > v_{\rm rms}$ at $(y-d)/\delta = 0.03$ (a point at the lower edge of the logarithmic layer). At the upper wall the frame of reference was rotated so that $v' > 0$ always corresponds to an ejection. We then accumulated statistics along y lines, at all the point where the condition was met, and also averaged in time. Both sweeps and ejections (as defined here) occurred at 10 to 15% of the points considered, but are associated with a Reynolds stress that is two or three times larger than the global average.

The conditioned statistics should differ from the global ones for a wall-normal distance equal to the correlation length of the coherent events causing the sweep or ejection. Figure 7 shows that, with no rotation, the wall-normal extent of the coherent motions that generate the sweeps and ejections is approximately $L_y = 0.1\delta$ (corresponding to 100-150 wall units), consistent with the expected size of the quasi streamwise vortices that are known to be responsible for these motions (Robinson, 1991). When rotation is applied, however, the size of these coherent motions extends much farther from the wall. This may be another effect of the advection due to the large roll cells.

When rotation is applied, sweeps become predominant on the stable side, ejections on the unstable one.

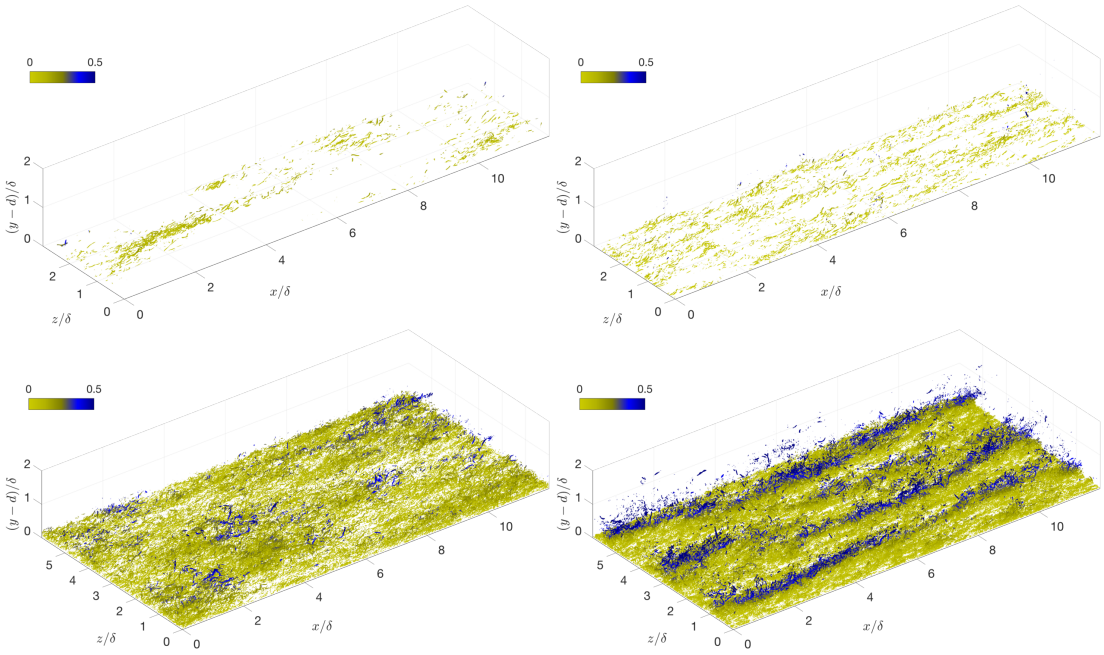

Figure 6: Isosurfaces of $\lambda_2 = -50$ (normalized by the local u_τ), coloured by distance from the wall, for $Ro = 0.42$. Top row: Smooth wall; bottom row: rough wall. Left column: Stable side; right column: unstable side.

Roughness intensifies the sweeps, consistent with previous findings that roughness leads to head-down hairpins that generates Q4 motions($u' > 0$, $v' < 0$) upstream of a roughness element (Talapatra & Katz, 2012). Thus, the difference between the stress due to the sweeps and that caused by the ejections is reduced. Roughness also causes the peak of the sweep contribution to move closer to the wall.

It has been observed that the form-induced perturbations can play an important role in modulating turbulence response to mean distortions in non-canonical wall-bounded flows, such as oscillatory channel flows (Ghodke & Apte, 2016) and spatially accelerating boundary layers (Yuan & Piomelli, 2015). For the present rotating channels, the wall-normal Reynolds stress budgets of the smooth and rough cases with $Ro_b = 1.0$ are compared in Figure 8. Despite significant wake kinetic energy in the roughness sublayer on both sides (Figure 5), the wake-production (Mignot *et al.*, 2009), $P_w = \langle \widetilde{v''u_i''}\partial\widetilde{v}/\partial x_i \rangle$, remains small, essentially zero on the stable side; this is probably associated with the reduction of $\langle \widetilde{v}\widetilde{v} \rangle$ on this side. The fact that on the stable side pressure work balances the sum of dissipation and the rotation term indicates that, for the present rotating channel flows, the cause of the destabilized turbulence on the stable side when roughness is present is not the wake perturbation, but the redistribution of turbulent kinetic energy to v''-energy through three-dimensional P'' gradients generated by the roughness blockage.

4 Conclusions

We have performed direct numerical simulations of turbulent channel flows subjected to spanwise rotation, comparing smooth and rough surfaces. The Reynolds number, for the non-rotating case, is fairly high, $Re_\tau = 950$. This allows the fully rough regime to be achieved, while keeping blockage effects small (the roughness height is 4% of the channel half-height).

The destabilizing role played by the roughness is particularly evident on the stable, cyclonic, side of the channel. Significantly more energy is present in the v' and w' fluctuations, decreasing the flow anisotropy; this is similar to the non-rotating case. At the highest rotation rate examined, $Ro_b = 1.00$, roughness plays a very significant role: when the wall is smooth the shear stress $\langle u'v' \rangle$ vanishes, while it remains significant on the rough wall.

Rotation attenuates the dispersive stresses on the stable side; although they remain significant, their effect on the Reynolds stress budgets is limited, indicating that they are not the primary source of destabilization due to roughness, as they are in other flows.

Acknowledgments

Support from Hydro Québec, the Natural Sciences and Engineering Research Council of Canada (NSERC) and the Center for Advanced Computing is acknowledged. U.P. gratefully acknowledges the support of the Canada Research Chairs program.

References

BRETHOUWER, G. 2017 Statistics and structure of spanwise rotating turbulent channel flow at moderate Reynolds numbers. em J. Fluid Mech. **828**, pp. 424–458.

DURBIN, P. A. & PETTERSSON REIF, B. A. 2001 *Statistical theory and modeling for turbulent flows*, 1st edn. Wiley.

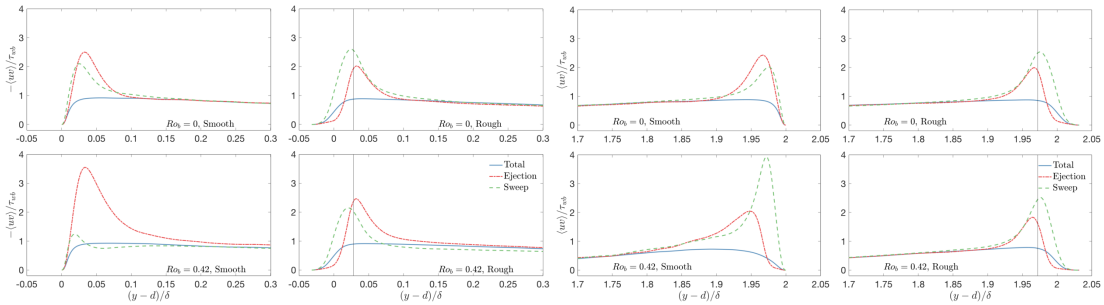

Figure 7: Conditionally averaged Reynolds shear stress $\langle u'v' \rangle$.

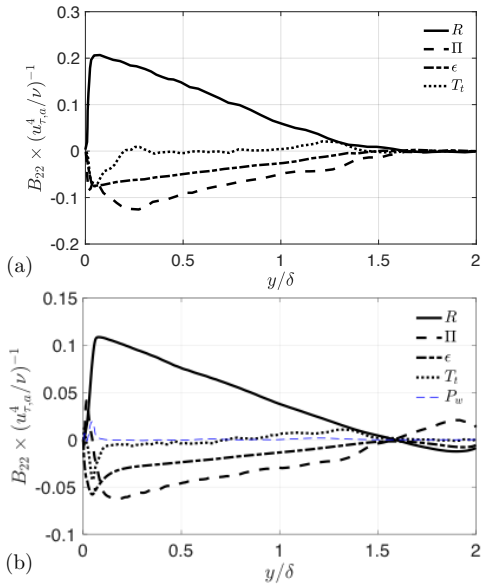

Figure 8: Budget balances of the wall-normal Reynolds stress with $Ro_b = 1.0$ for (a) smooth and (b) rough cases. R: Additional budget term due to rotation; Π: pressure work; ϵ: viscous dissipation; T_t: turbulent transport; P_w: wake production.

GHODKE, C. D. & APTE, S. V. 2016 DNS study of particle-bed–turbulence interactions in an oscillatory wall-bounded flow. *J. Fluid Mech.* **792**, 232–251.

GRUNDESTAM, O., WALLIN, S. & JOHANSSON, A. V. 2008 Direct numerical simulations of rotating turbulent channel flow. *J. Fluid Mech.* **598**, 177–199.

HOYAS, S. & JIMÉNEZ, J. 2006 Scaling of the velocity fluctuations in turbulent channels up to Re_τ=2003. *Phys. Fluids* **18**, 011702.

JEONG, J. & HUSSAIN, F. 1995 On the identification of a vortex. *J. Fluid Mech.* **285**, 69–94.

JOHNSTON, J. P., HALLEEN, R. M. & LEZIUS, R. K. 1972 Effect of spanwise rotation on the structure of two-dimensional fully developed turbulent channel flow. *J. Fluid Mech.* **56** (03), 533–557.

KRISTOFFERSEN, R. & ANDERSSON, H. I. 1993 Direct simulations of low-Reynolds-number turbulent flow in a rotating channel. *J. Fluid Mech.* **256**, 163–197.

LAMBALLAIS, E., LESIEUR, M. & MÉTAIS, O. 1996 Effects of spanwise rotation on the vorticity straining in transitional and turbulent channel flows. *Int. J. Heat Fluid Flow* **17**, 324–332.

LAMBALLAIS, E., MÉTAIS, O. & LESIEUR, M. 1998 Spectral-Dynamic Model for Large-Eddy Simulations of Turbulent Rotating Channel Flow. *Theor. Comput. Fluid Dyn.* **12** (3), 149–177.

MACIEL, Y., PICARD, D., YAN, G., DUMAS, G. & GLEYZES, C. 2003 Fully developed turbulent channel flow subject to system rotation. *AIAA Paper 2003-4153*.

MIGNOT, E., BARTHELEMY, E. & HURTIER, D. 2009 Double-averaging analysis and local flow characterization of near-bed turbulence in gravel-bed channel flows. *J. Fluid Mech.* **618**, 279—303.

NAKABAYASHI, K. & KITOH, O. 1996 Low Reynolds number fully developed two-dimensional turbulent channel flow with system rotation. *Journal of Fluid Mechanics* **315** (1), 1–29.

NAKABAYASHI, K. & KITOH, O. 2005 Turbulence characteristics of two-dimensional channel flow with system rotation. *J. Fluid Mech.* **528**, 355–377.

NARASIMHAMURTHY, V. D. & ANDERSSON, H. I. 2015 Turbulence statistics in a rotating ribbed channel. *Int. J. Heat Fluid Flow* **51**, 29–41.

PERRY, A. E. & JOUBERT, P. N. 1969 Rough wall turbulent boundary layers. *J. Fluid Mechanics* **37** (02), 193–211.

ROBINSON, S. K. 1991 Coherent motions in the turbulent boundary layer. *Annu. Rev. Fluid Mech.* **23** (1), 601–639.

SCOTTI, A. 2006 Direct numerical simulation of turbulent channel flows with boundary roughened with virtual sand-paper. *Phys. Fluids* **18**, 031701.

TAFTI, D. K. & VANKA, S. P. 1991 A numerical study of the effects of spanwise rotation on turbulent channel flow. *Phys. Fluids A* **3** (4), 642–656.

TALAPATRA, S. & KATZ, J. 2012 Coherent structures in the inner part of a rough-wall channel flow resolved using holographic piv. *J. Fluid Mech.* **711**, 161–170.

XIA, Z., SHI, Y. & CHEN, S. 2016 Direct numerical simulation of turbulent channel flow with spanwise rotation. *J. Fluid Mech.* **788**, 42–56.

YUAN, J. & PIOMELLI, U. 2014*a* Numerical simulations of sink-flow boundary layers over rough surfaces. *Phys. Fluids* **26**, 015113–1–28.

YUAN, J. & PIOMELLI, U. 2014*b* Roughness effects on the Reynolds stress budgets in near-wall turbulence. *J. Fluid Mech.* **760**, R1–1–12.

YUAN, J. & PIOMELLI, U. 2015 Numerical simulation of a spatially developing accelerating boundary layer over roughness. *J. Fluid Mech.* **780**, 192–214.